

Stability and decay of subradiant patterns in a quantum gas with photon-mediated interactions

Alexander Baumgärtner,^{1,2,*} Simon Hertlein,^{1,*} Tom Schmit,^{3,*} Davide Dreon,¹
 Carlos Máximo,^{1,4} Xiangliang Li,^{1,5} Giovanna Morigi,³ and Tobias Donner^{1,†}

¹*Institute for Quantum Electronics, Eidgenössische Technische Hochschule Zürich, Otto-Stern-Weg 1, CH-8093 Zurich, Switzerland*

²*Current address: JILA, University of Colorado and National Institute of Standards and Technology, and Department of Physics, University of Colorado, Boulder, Colorado 80309, USA*

³*Theoretical Physics, Saarland University, Campus E2.6, D-66123 Saarbrücken, Germany*

⁴*Current address: Departamento de Física, Universidade Federal de São Carlos, 13565-905 São Carlos, São Paulo, Brazil*

⁵*Current address: Beijing Academy of Quantum Information Sciences, Xi-bei-wang East Road No.10, 100193 Beijing, China*

(Dated: July 15, 2024)

The phenomenon of subradiance, marked by its surprising suppression of spontaneous emission, challenges conventional expectations of the collective behavior of scatterers. We study subradiance in the experimental setting of a Bose-Einstein condensate positioned at the mode crossing of two optical cavities. In this setup, subradiance manifests in the form of metastable density structures that suppress emission into one cavity mode, thereby preventing relaxation to the stationary, superradiant grating that minimizes the system’s energy. We observe lifetimes of the subradiant states exceeding hundred milliseconds, far surpassing any characteristic dynamic time scale of the system. Eventually, an instability triggers a rapid transition to the superradiant stationary pattern. We reproduce these dynamics by a quantum mean field model, suggesting that subradiance shares characteristics with quasi-stationary states predicted in other long-range interacting systems such as astrophysical clusters and plasmas. This behavior highlights the potential of photon-mediated long-range forces as controllable and exploitable quantum cooperative phenomenon.

The radiative properties of a collection of scatterers can manifest features that are hardly explained by the dynamics of the individual constituents, but rely on their interplay [1, 2]. Two prime examples are subradiance and superradiance, which result from the destructive and constructive interference, respectively, of electromagnetic fields radiated from the emitters [3, 4]. In the simplest case of two dipoles, subradiance results from their antisymmetric superposition such that they oscillate out of phase, effectively decoupling them from the electromagnetic environment, and leading to vanishing emission rates [5–12]. The counterpart, superradiance, is rooted in the symmetric superposition of atomic states, leading to enhanced emission rates. While superradiance has been realized in diverse systems [4, 13], subradiant states of ensembles of emitters are intrinsically hard to prepare and observe [14–16]. Only few realizations exist including the recent demonstrations in a disordered ensemble of cold atoms [17], in a single layer of atoms pinned in an optical lattice [18], and in a tweezer array of a few atoms positioned within an optical cavity [19].

Rather than coupling radiation to the excited electronic states, one can also use the emitter’s center-of-mass motion momentum states and couple them via Raman transitions. The relative phase of the light emitted by the scatterers dictates the collective interference and can, for instance, be determined by the linear momen-

tum of free electrons [20] or of a Bose-Einstein condensate (BEC) [21]. Superradiant bursts of light have been observed using an elongated BEC to scatter light, resulting in the population of well-defined atomic momentum states and the formation of a Bragg grating [21]. Similarly, subradiance has been demonstrated using momentum states of a BEC coupled to a recoil-resolving optical cavity [22, 23]. Scattering here was suppressed due to a frequency mismatch between the light scattered off the accelerated atoms and the narrow-band resonator.

Superradiance is usually associated with an instability. The Dicke model, however, also predicts a phase transition to a stationary superradiant phase [24–27]. This transition occurs above a critical coupling between the emitters and a mode of the electromagnetic field. In the first experimental realization [28], the superradiant phase corresponds to the formation of a self-ordered matter-wave grating of a BEC, that maximizes the coherent scattering of an illuminating field into a single mode of an optical cavity. In this phase the cavity photons effectively mediate global optomechanical forces between the atoms, which stabilize the pattern in a self-consistent fashion [29–32]. On the contrary, for the very nature of subradiance, subradiant patterns are unstable, since the forces vanish with the field. Stable subradiant patterns can only occur in the presence of a second external potential localizing the atoms at positions where emission into the cavity mode is suppressed [10, 19, 33, 34]. Such a pinning potential creates a density modulation, which results in the atoms forming a photonic material with the cavity mode situated within the bandgap [35].

* these authors contributed equally

† donner@phys.ethz.ch

In this work, we realize a subradiant many-body phase where a pinning potential, which stabilizes the subradiant pattern and inhibits scattering into a primary cavity, is itself provided by a self-organized potential supported by a secondary cavity. The subradiant state is prepared through an experimental protocol changing the relative detunings of the cavities. We observe that the atoms remain locked in the initial pattern that suppresses emission into the primary cavity, even though this state is energetically unfavorable. The lifetimes of these metastable subradiant configurations exceed any characteristic timescale of the dynamics and are solely limited by atom losses. Their decay is not gradual but rather occurs as an instability, at which the atomic density suddenly switches into a superradiant, stationary grating that scatters into the first cavity.

These features make subradiance in cavity self-organization notably different from free space, where decay typically follows a power-law behavior [17]. We present a theoretical model which aligns with the experimental findings, demonstrating that the subradiant state is the fixed point of a nonlinear equation with few parameters. The classical limit is described by the Vlasov equation, which governs the instability of strong long-range systems like plasmas [36, 37] and gravitational clusters [38]. The observed behavior exhibits characteristics of violent relaxation, typical for instabilities in such systems [36–38], underscoring the paradigmatic nature of strong long-range interacting systems.

System description

The setup is composed of two high-finesse optical cavities ($\nu = 1, 2$) that cross under an angle of 60° , see Fig. 1a. A BEC of $N = 2.7(3) \cdot 10^5$ ^{87}Rb atoms is placed in a dipole trap located at the crossing point of the modes. The cavities are characterized by their couplings $g_{\nu=1,2}/2\pi = (1.95, 1.77)$ MHz and field decay rates $\kappa_{\nu=1,2}/2\pi = (147, 800)$ kHz. In the plane spanned by the cavities, the atoms are illuminated by a standing wave laser at frequency ω_p and with Rabi frequency Ω . This pump field is far blue detuned by $\Delta_a = \omega_p - \omega_a = 2\pi \times 69.8(1)$ GHz with respect to the atomic resonance frequency ω_a . It forms a repulsive optical lattice potential of depth $V_p = \hbar\Omega^2/\Delta_a$ that tends to localize the atoms at the nodes (\hbar is the reduced Planck constant). The dispersive dynamics of the BEC-cavity system gives rise to the self-consistent formation of atomic density gratings that scatter light into the cavity and cause a shift in the cavity frequencies. The strength of these processes can be controlled by the detunings $\Delta_\nu = \omega_p - \omega_\nu^c$ between the driving laser field and the respective cavity resonance [39].

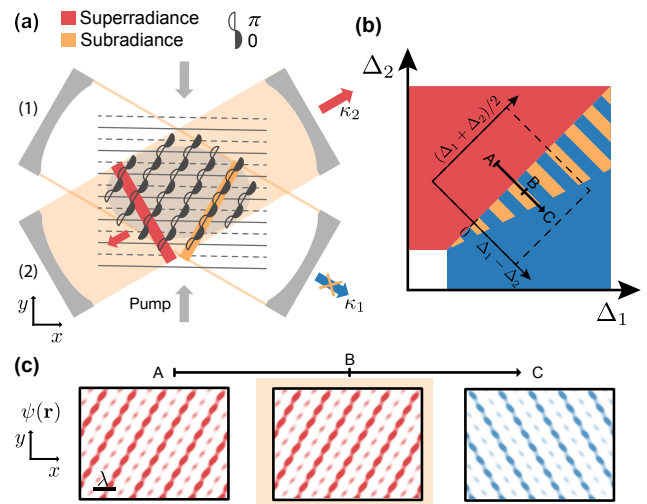


FIG. 1. **Subradiant state of a Bose-Einstein condensate in two crossed cavities.** (a) BEC (grey oval) coupled to two optical cavities and a transverse pump lattice (grey dashed and solid lines indicate the phase of the pump). The black wave pattern displays the density of the self-ordered atoms scattering light, where atoms at open symbols scatter light π out of phase with respect to atoms at filled symbols. The atoms emit in phase (red bar) into cavity (2), while emission into cavity (1) is suppressed due to destructive interference (yellow bar), eventually resulting in subradiance. (b) Conceptual phase diagram as a function of detunings Δ_1, Δ_2 between pump and the respective cavity and at fixed pump amplitude. The colors indicate the cavity that exhibits a non-vanishing light field. Preparing the system in point A and changing detunings via B to C, it passes a subradiant phase (red/orange stripes) where cavity (2) is still occupied with photons, before switching to emission in cavity (1). The dashed rectangle shows the coordinate system used in the subsequent figures. (c) Real space distributions of the self-ordered atomic patterns for each point (A, B, C) indicated in panel (b).

Stationary Phase Diagram

Figure 1b illustrates the stationary phase diagram as a function of the detunings Δ_ν for a fixed pump strength V_p . The white region is the normal phase, while the blue and red regions correspond to a field in cavity 1 and 2, respectively. Subplot (c) shows the atomic configurations at the corresponding points in the red (A) and blue (C) regions, showcasing stripe pattern formations conducive to coherent superradiant emission into the respective cavity mode. The atomic density extends to regions where the repulsive pump lattice is maximal. However, the configuration is facilitated by the cavity field: at the stripes, cavity and laser destructively interfere [40], and the resulting optomechanical potential is reduced. This mechanism is the optomechanical analog of the dynamics of localized dipoles in cavities [34, 41]. The emerging patterns are such that superradiant emission into the two cavities is mutually exclusive for sufficiently low pump

strengths.

In order to experimentally determine the steady state phase diagram, we fix the detunings Δ_1, Δ_2 and then linearly increase the pump lattice depth V_p up to a target value [42]. We then record in real time the light leaking from the cavities using two heterodyne detection setups. The left panels of Fig. 2 show the measured phase diagrams for two target values of the pump amplitude as a function of the relative cavity detuning $(\Delta_1 - \Delta_2)$ and the mean cavity detuning $(\Delta_1 + \Delta_2)/2$. We observe three regimes: For low pump lattice depths no self-ordering takes place and the cavities remain dark. For a large range of intermediate pump lattice depths, exclusively the cavity with the lower absolute detuning Δ_ν is filled with light, see Figure 2a. Absorption images, taken after suddenly switching off all light fields and ballistic expansion of the BEC, confirm that the self-ordered states form stripes oriented to optimally scatter into the populated cavity mode. Finally, for very deep pump lattices a region of coexistence becomes possible, where both cavities are populated simultaneously, see the grey region in Figure 2c.

The experimental phase diagrams are reproduced by the ground state of a modified Gross-Pitaevskii equation, for the macroscopic wave function ψ of the condensate in two dimensions,

$$i\hbar\partial_t\psi = \left(-\frac{\hbar^2\vec{\nabla}^2}{2m} + \sum_{\nu=x,y} \frac{1}{2}m\omega_\nu^2\nu^2 + V_0N|\psi|^2 + \hat{H}_{\text{mf}}[\psi] \right) \psi, \quad (1)$$

where V_0 is the s -wave, contact potential and \hat{H}_{mf} describes the optical potential in the mean-field approximation [42]. For blue atomic detuning, $\Delta_a > 0$, the optical potential can be cast into the form

$$\hat{H}_{\text{mf}}[\varphi]/\hbar = \left(\sqrt{V_p}\hat{\rho}_p + \sum_{\nu=1}^2 \sqrt{U_\nu}\alpha_\nu\hat{\theta}_\nu \right)^2, \quad (2)$$

which takes always positive values. Here, $U_\nu = g_\nu^2/\Delta_a > 0$ denotes the dispersive Stark per particle shift due to the coupling with cavity mode $\nu = 1, 2$. The variables $\alpha_\nu[\psi]$ are the electric field amplitudes of cavity mode ν and depend on the atomic density distribution. Finally, the phase-matching conditions are determined by operators $\hat{\theta}_j = \cos(\vec{k}_j \cdot \vec{x})$ (with $j = p, 1, 2$) which capture the overlap between atomic density and the wave vector \vec{k}_j of the pump beam or the respective cavity.

The potential energy $E_{\text{mf}} = \langle \hat{H}_{\text{mf}} \rangle$ is always positive. It is minimized when the intracavity field amplitudes cancel out the pump field. At fixed pump field V_p this sets a constraint on the maximal values of the intracavity fields. Energy minimization of the full Hamiltonian, together with this constraint, leads to two thresholds [42]. A lower threshold value, for which it is energetically favourable

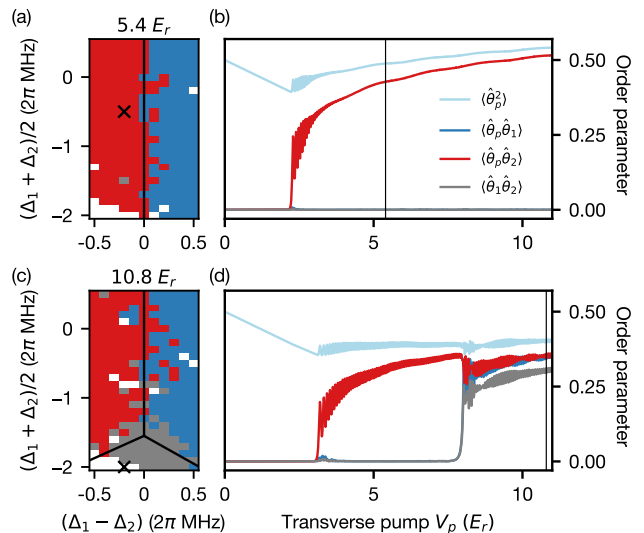


FIG. 2. **Phase diagrams.** (a,c) Experimental steady state phase diagrams for pump lattice depths $V_p = (5.4, 10.8) E_r$, with $E_r = 2\pi\hbar \times 3.77$ kHz. The blue (red) color indicates light exclusively in cavity 1 (2), white the absence of light, while the grey denotes coexistence, where atoms scatter in both cavities simultaneously. Black lines mark the phase boundaries calculated from GPE simulations. The crosses in a,c indicate detunings where b,d were simulated. A systematic error of 0.1 MHz in the cavity detunings has been taken into account [42]. (b,d) GPE simulations of the expectation values of the order parameters $\langle \hat{\theta}_j \hat{\theta}_k \rangle$ with $j, k = p, 1, 2$ as a function of lattice depth V_p . Vertical lines mark the lattice depths of panels a,c. Increasing V_p initially leads to decreasing $\langle \hat{\theta}_p^2 \rangle$, until self-ordering sets in and atoms are pulled towards the intensity maxima of the repulsive lattice potential. In panel (d) both thresholds for self-ordering in cavity 2 and in both cavities are visible.

that the system self-organizes in the cavity mode with the largest coupling strength $C_\nu = U_\nu N/\Delta_\nu$. Here, the atoms form stripes maximizing the order parameter $\langle \hat{\theta}_p \hat{\theta}_\nu \rangle$, see Figure 1a. At the second, higher threshold, simultaneous self-organization in both cavity modes becomes mechanically stable, such that the atoms form a pattern maximizing $\langle \hat{\theta}_1 \hat{\theta}_2 \rangle$. The two thresholds are visible in the numerical simulation shown in Figure 2d. In the rest of this work we will focus on pump strengths between the two threshold values, where the two types of order ($\langle \hat{\theta}_p \hat{\theta}_1 \rangle, \langle \hat{\theta}_p \hat{\theta}_2 \rangle$) compete. Self-organization will take place in the more strongly coupled cavity mode, hence, for constant pump strength, the ratio C_1/C_2 , and thus the experimental parameters (Δ_1, Δ_2) , determines the stationary phase.

Formation of Subradiant States

Having two competing superradiant crystals allows us to explore the transition between these structures *in-situ*,

where we vary the cavity mode resonance frequencies, and thus the detunings Δ_1 and Δ_2 , as a function of time and at constant pump lattice depth. In our protocol, we initialize the system in a superradiant state in one of the cavities, such as cavity 2, by setting $\Delta_1 > \Delta_2$, increasing the lattice depth V_p within 5 ms, and then keeping it constant. At $t = 5$ ms, we linearly change the relative cavity detuning $(\Delta_1 - \Delta_2)$ over 25 ms to the inverse situation, $\Delta_1 < \Delta_2$, while maintaining a constant mean detuning $(\Delta_1 + \Delta_2)/2$. A typical trace of the cavity occupations is displayed in Figure 3a. The atoms self-organize within cavity 2 during the initial ramp up of the drive. At 5 ms, the photon number in cavity 2 decreases again since the effective coupling C_2 decreases during the sweep of the relative detuning. The phase diagram (Figure 2a) predicts that the state of the system should change the superradiant emission from one cavity to the other at $\Delta_1 \approx \Delta_2$. However, we observe a pronounced hysteretic behavior, indicated by the orange shading. Only past this point of balanced coupling the system changes emission into the other cavity. Here the photon number increases since the coupling to that cavity is increased over time. In Figure 3b, we show data for different detunings. The size of the hysteresis depends monotonously on the mean cavity detuning; the stronger the atoms are effectively coupled to the cavities, the larger is the hysteresis.

This hysteretic behavior is a manifestation of the discontinuous transition between the two self-organized phases. In the bistable regime the atoms do not reorganize into the pattern that minimizes the energy by scattering superradiantly in the other cavity mode, but instead remain localized in a pattern that suppresses scattering into this very mode. We identify this as a subradiant state where the atoms form a crystal such that emission into the more strongly coupled mode is suppressed by destructive interference. The system remains stably in this subradiant state until the coupling to the second cavity is sufficiently strong. Then, the cavity mode population abruptly changes, indicating a quick reorganization of the atomic structure.

The numerical simulations of this dynamics using the GPE of Eq. (1) predict a hysteresis region that qualitatively reproduces the experimental measurement. The size of the theoretical hysteresis is however larger, as visible in Figure 3b. We attribute this discrepancy to the model's inability to capture several experimental features. These include noise in the detunings Δ_ν , as well as a finite spatial overlap between the BEC and the two cavity mode functions, whose mode waists are located at slightly different spatial points, resulting in an inhomogeneous model and likely atomic currents during the ramp. The rates associated with contact interactions and trap oscillations, in particular, are larger than the rate of the slow ramp, and are thus expected to influence the relaxation dynamics. This hypothesis is verified by comparison with numerical simulations that discard the contact interactions and the trap in the dynamics, which use Eq.

(1) setting $\omega_\nu = 0$ and $V_0 = 0$ but keep the cavity potential and the pump. In this limit the GPE is reduced to a form known as Generalized GPE (GGPE) [43], where the sole interactions are of global range [42]. The initial state is inhomogeneous and the predictions of the GGPE are very sensitive to small density fluctuations. They generally result in a smaller hysteresis region than the experiment. Comparing the results of the GPE and of the GGPE allow to single out the effect of contact interactions and trap potential and shows that these factors tend to stabilize the subradiant state. We conjecture that their effect is to suppress the onset of large density fluctuations during the ramp, which otherwise seed a radiative instability.

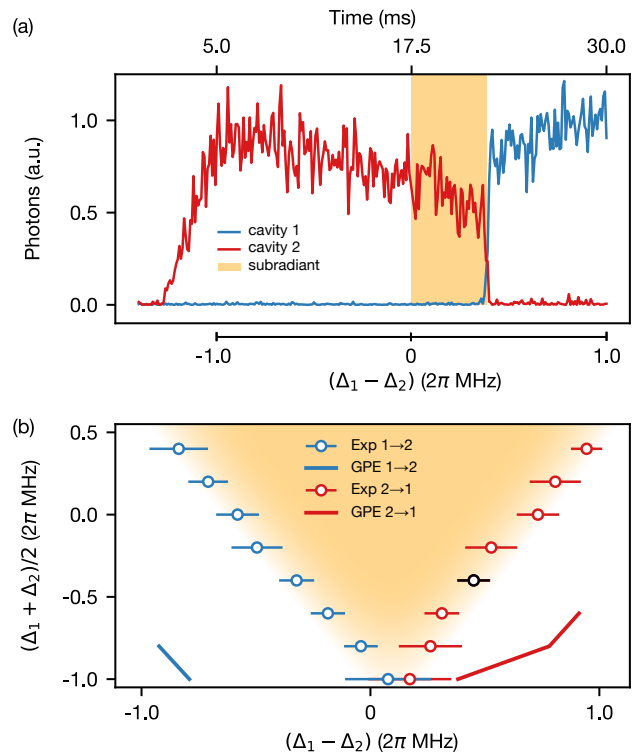


FIG. 3. **Hysteresis Measurement.** (a) Real time evolution of the cavity occupations. In the first 5 ms, V_p is ramped to $8.8 E_r$ at fixed detunings. Afterwards, V_p and the mean detuning $(\Delta_1 + \Delta_2)/2$ are kept constant, but the relative detuning $(\Delta_1 - \Delta_2)$ is ramped in time, passing the point $\Delta_1 = \Delta_2$ at 17.5 ms (see lower axis of this plot). The cavity populations only switch past this point at a positive relative detuning, indicating subradiant, hysteretic behavior (orange color). (b) Switching points extracted from data sets as shown in panel (a) as a function of the mean detuning $(\Delta_1 + \Delta_2)/2$. Errorbars display the standard deviation, the orange shading indicates the metastable region of subradiance observed experimentally. The black data point indicates detunings at which data in panel (a) was taken. The solid lines show results from GPE simulations, which predict a far broader region of hysteresis than observed in the experiment. For most mean detuning values, the GPE simulation does not predict any switch out of the subradiant state within the simulation time.

Lifetime of Subradiant States

We now analyse the stability of the subradiant states by preparing them using quenches, namely, by suddenly tuning the cavity detunings across the phase diagram so that a stable superradiant pattern becomes an excited, subradiant state. Experimentally, we initialize the system in the superradiant state with respect to cavity 2 by ramping up the drive field within 10 ms to $4.2 E_r$ at fixed detunings $(\Delta_1, \Delta_2) = (\delta, 0)$ and then abruptly swap detunings between the cavities to $(\Delta_1, \Delta_2) = (0, \delta)$. We observe that the system keeps emitting into cavity 2, and thus remains in the pattern that suppresses emission into cavity 1, entering a subradiant phase. Depending on the quench parameter δ , the BEC eventually reorders after a finite time into the superradiant state, emitting light exclusively into cavity 1. We extract the lifetime of the subradiant state by fitting the time at which the cavity field occupations swap (see Figure 4c and e).

Figure 4a shows the measured lifetimes of the subradiant states as a function of the quench strength δ . We identify four prominent features: (i) the lifetimes exceed any dynamic timescale of the system's constituents: The observed lifetimes are only compatible with the atom loss rate which is on the order of 3 Hz, see [42]. (ii) The instability is characterized by a switch from the metastable subradiant to the stationary superradiant pattern, thereby preserving superfluidity, as can be seen from the absorption images in Figure 4d and f. (iii) The transition itself is very fast with respect to the characteristic energy of trapping potential, contact interaction, and quantum fluctuations. Moreover, it does not have features of nucleation. (iv) During the transition we observe emission in both cavity modes, see Figure 2. Interestingly, the corresponding pattern is energetically costly and would only become stable for higher pump strengths and smaller detunings.

These features are consistent with the dynamics of meta-stabilities and instabilities of long-range interacting systems. The short-time behavior of the transition is typical of Vlasov instabilities in plasmas and gravitational systems [44–47], and have been predicted in theoretical studies of relaxation of laser-cooled atoms in resonators [30, 48]. These instabilities have a characteristic exponential amplification of fluctuations (“violent relaxation”) [37, 45, 49] and can be triggered by a change of the energy [50], which in our case is slowly ramped down by atom losses. The transient, simultaneous emission into both cavity modes is consistent with the tendency of long-range interacting systems to suppress the formation of domains and thereby minimize the long-range potential term [32, 51]. Finally, superfluidity is expected to be preserved since the long-range interaction term of Eq. (1) does not affect off-diagonal long-range order.

Following this conjecture, we analyse the predictions of the quantum Vlasov equation, which we derive from the GGPE. Instability are identified from the the short-time dynamics of linear fluctuations $\delta\psi$ about the equilibrium

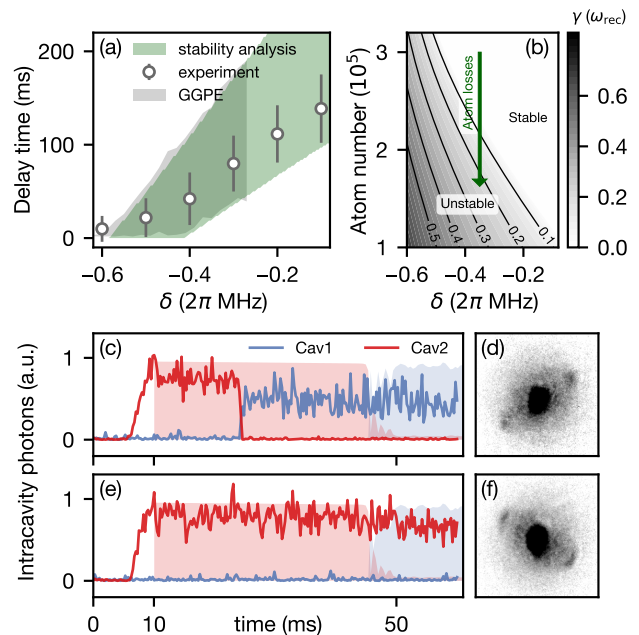


FIG. 4. **Lifetime of subradiant states.** (a) After preparing the system in a superradiant state of cavity 2 at $V_p = 4.2 E_r$, the relative detuning is quenched from $(\Delta_1, \Delta_2) = (\delta, 0)$ to $(0, \delta)$. The system becomes subradiant with respect to cavity 1 until it eventually switches to a superradiant state with respect to cavity 1. We display the delay time for which the system remains in the subradiant state as function of quench strength δ . The grey area represents the GGPE simulation results, while the green area displays the results of our stability analysis. Both theory results span from the maximum atom number (minimum atom loss) to the minimum atom number (maximum atom loss). (b) Escape rates out of the subradiant state derived from the mean field model as function of relative detuning and atom number. Atom loss eventually forces the system to leave the subradiant state for otherwise fixed parameters. (c,e) Two exemplary real-time traces of the cavity occupations from the data in panel (a) for identical parameters $\delta = 2\pi \times -0.4$ MHz: For the initial 10 milliseconds, cavity 2 is prepared in a superradiant state. After the quench, the system decays in the superradiant state of cavity 1 (c) or remains in the subradiant state for longer times (e). In the background (filled areas) we show a dynamical GGPE simulation for these parameters, initialized as superradiant state in cavity 2 at 10 ms. (d,f) Absorption images of the atomic momentum distributions at the end of the traces displayed in panels (c,e), respectively.

state ψ_0 , which is governed by the equation [42]

$$\omega \delta\psi = \left(\frac{\hbar^2 \vec{\nabla}^2}{2m} - H_{\text{mf}}[\psi_0] \right) \delta\psi - \delta H_{\text{mf}}[\psi_0] \psi_0,$$

where $\delta H_{\text{mf}}[\psi_0]$ represents the variation of the mean-field potential around the subradiant state and the number of atoms N enters $H_{\text{mf}}[\psi]$ as a time-dependent, slowly decaying variable, as illustrated in Fig. 4(b). The instability is signalled by $\text{Im}\omega < 0$, allowing us to identify a

threshold value N_c below which the subradiant state becomes unstable. Above threshold, the subradiant state is a stable solution of the quantum Vlasov equation, and a quasi-stationary state of long-range interacting systems [37, 52, 53]. Below this threshold, the system quickly escapes out of the subradiant state with exponential growth at rate $\gamma = -\text{Im}\omega$, typical of violent relaxation. The results of this analysis are reported in Fig. 4(a) and are in agreement with the experimental data, showing that this simplified model captures the essential features. The instability is seeded by quantum fluctuations of the atoms' kinetic energy in the repulsive potential. Due to the superfluid properties of the subradiant state, this is a rare experimental example of a *quantum* quasi-stationary state. While the Vlasov equation approximates the short time dynamics of the GGPE, the full GGPE captures how the system reaches the superradiant phase. Figure 4(c,e) shows the agreement between the photon traces of experiment and theory within the uncertainty in the atom loss rate. When the simulations include contact interactions and trap potentials, we find the lifetime of the subradiant state to be larger yet within the same order of magnitude. This confirms that the relaxation dynamics is primarily governed by the interplay of quantum fluctuations, which initiate the transition, and long-range interactions, which determine the instability and drive the system into the stable, superradiant state. In both cases, the final state aligns with experimental observations, demonstrating that long-range interactions dominate the overall dynamics throughout the instability.

Conclusions

We have investigated the relaxation dynamics of a quantum Bose gas with competing global-range interactions mediated by photons. These interactions impose two competing spatial patterns, leading to a phase diagram which we have explored by tuning the cavity frequencies. The transition between the two configurations is of first order. A slow ramp across that transition reveals a typical hysteretical behavior: within the hysteresis region the gas remains trapped in the pattern that suppresses emission in the other cavity, forming a subradiant grating. At the instability, it quickly reorders into the superradiant pattern. Energy considerations show that the reordering mechanism is dominated by the global-range interactions, as expected. Our theoretical study indicates that the breadth of the hysteresis region can be reproduced quantitatively only by taking into account fine-tuned contact interactions and spatial inhomogeneities, going beyond the scope of this work: Even if these processes are characterized by significantly slower timescales, for slow ramps their interplay with the global forces control the density fluctuations that seed the instability.

The relaxation following sudden quenches across the phase diagram, instead, is solely governed by the inter-

play of global forces and kinetic energy. We identified parameter regimes where the subradiant patterns are excited stable states, and exhibit features of the quasi-stationary states of plasmas and gravitational clusters. Their lifetime is limited only by atom losses which slowly reduce the strength of the interactions, and thus the energy. Similar mechanisms have been discussed in the literature of ideal models [50, 54], for which our many-body cavity QED setup provides a test.

The observed instability is seeded by density fluctuations due to the kinetic energy and exhibits characteristics of a violent relaxation, typical of the Vlasov equation. Differing from simulations with optical systems [55], the instability emerges from the many-body dynamics of ultracold bosons that interact via multiple photon scattering. Our findings can thus also be connected to the non-equilibrium dynamics of ultracold Fermions with photon-mediated interactions in vicinity of a second order phase transition. There, relaxation to a stationary was observed within less than a millisecond, but with typical features of a dynamical instability [56–58]. Such characteristics are thus distinctive of instabilities in long-range interacting systems across various length scales and in this sense universal.

Despite the complexity of the system, the relative simplicity of our model allows us to unveil the microscopic dynamics at work: The quasi-stationary state is stabilized by the destructive interference between scattering of photons into pump and cavity mode, suppressing emission into the second cavity. Its instability is triggered by a loss mechanism that reduces the long range coupling, and thus lowers the self-organized potential that traps the atoms. Despite the energy quench, the gas remains superfluid across the transition and the quasi-stationary state is a quantum phase of matter.

Our results shed light on the individual mechanisms at work and on their interplay. By establishing a direct connection between the microscopic dynamics and the macroscopic observation we provide an example of universal behavior in the out-of-equilibrium dynamics. Our work demonstrates the potential of many-body cavity quantum electrodynamics to unveil the processes leading to relaxation in long-range interacting systems. Moreover, by validating the simplified model for the out-of-equilibrium dynamics, this study lays the foundation for a toolkit to control metastable quantum states in many-body systems.

ACKNOWLEDGMENTS

The authors acknowledge stimulating discussions with Immanuel Bloch, Tilman Esslinger, Stefan Ostermann, and Susanne Yelin. This work was funded by the Deutsche Forschungsgemeinschaft (DFG, German Research Foundation) – Project-ID 429529648 – TRR306 QuCoLiMa (“Quantum Cooperativity of Light and Matter”), the DFG and Swiss National Science Foundation

(SNSF) Forschergruppe WEAVE "Quantum many-body dynamics of matter and light in cavity QED" - DFG project ID 525057097, SNSF project number 217124, the QuantERA project "QNet: Quantum transport, metastability, and neuromorphic applications in Quantum Networks" - DFG project ID 532771420, SNSF project number 221538, and the SNSF project 186312

on "Cavity-assisted pattern recognition". This research was supported in part by the National Science Foundation under Grants No. NSF PHY-1748958 and PHY-2309135. We further acknowledge funding from the Swiss State Secretariat for Education, Research and Innovation (SERI).

Supplemental Materials

Appendix A: Theoretical Model: Gross-Pitaevskii equation with global-range interactions

In this Appendix, we provide details about the theoretical model of the system and the numerical simulations we performed, leading to the data presented in the main text. In the first section, we introduce the full quantum mechanical model of atoms and cavities. By adiabatically eliminating the cavities' degrees of freedom and employing a mean-field ansatz for the state of the atomic sector, we derive in the subsequent sections a mean-field Hamiltonian, which is at the center of our theoretical model. At the end, we give additional information about its numerical implementation.

1. Quantum master equation for the composite system

The starting point for the derivation is the quantum master equation describing the dynamics of the two cavity modes ($\nu = 1, 2$) and the motional degrees of freedom of the particles, obtained by adiabatically eliminating the atoms' internal degrees of freedom [40]:

$$\frac{\partial}{\partial t} \hat{\rho} = -\frac{i}{\hbar} \left[\hat{H}_a + \hat{H}_f + \hat{V}_{\text{int}}, \hat{\rho} \right] + \sum_{\nu=1}^2 \kappa_{\nu} \mathcal{L}[\hat{a}_{\nu}] \hat{\rho}. \quad (\text{A1})$$

The incoherent dynamics consists of the cavity losses, characterized by the population decay rates $\kappa_{\nu=1,2}$ and described by the superoperator $\kappa_{\nu} \mathcal{L}[\hat{a}_{\nu}] \hat{\rho} = \kappa_{\nu} (2\hat{a}_{\nu} \hat{\rho} \hat{a}_{\nu}^{\dagger} - \hat{a}_{\nu}^{\dagger} \hat{a}_{\nu} \hat{\rho} - \hat{\rho} \hat{a}_{\nu}^{\dagger} \hat{a}_{\nu})/2$. Here, \hat{a}_{ν} and \hat{a}_{ν}^{\dagger} are the annihilation and creation operators of cavity ν , obeying the bosonic commutation relations $[\hat{a}_{\nu}, \hat{a}_{\mu}^{\dagger}] = \delta_{\nu,\mu}$ and $[\hat{a}_{\nu}, \hat{a}_{\mu}] = 0$. In the dispersive limit, where the atomic detuning from the pump laser Δ_a dominates the radiative losses of the atoms γ [59], that is, $|\Delta_a| \gg \gamma$, the interaction of the particles with the pump and cavity fields is essentially coherent on the typical timescale of the experiment. The (effective) Hamiltonians describing the coherent free dynamics of the N particles (\hat{H}_a) and the cavity modes (\hat{H}_f) read (in the frame rotating with the pump frequency ω_p)

$$\hat{H}_a = \sum_{j=1}^N \left(\frac{\hat{p}_j^2}{2m} + \hbar V_p \cos^2(\vec{k}_p \cdot \hat{x}_j) \right) \quad \text{and} \quad \hat{H}_f = -\sum_{\nu=1}^2 \hbar \Delta_{\nu} \hat{a}_{\nu}^{\dagger} \hat{a}_{\nu}. \quad (\text{A2})$$

Here, $V_p = \Omega^2/\Delta_a$ is the pump lattice depth, controlled by the Rabi frequency Ω of the laser and the atomic detuning Δ_a , and \vec{k}_p is the wavevector of the pump laser. Without loss of generality, we choose the pump axis to be the y -axis of our two-dimensional coordinates system, that is, $\vec{k}_p = |\vec{k}_p| \vec{e}_y$. The interaction of the particles with the cavity modes (\hat{V}_{int}) is given for a blue-detuned atomic detuning, $\Delta_a > 0$, by

$$\hat{V}_{\text{int}} = \sum_{\nu=1}^2 \hbar U_{\nu} \hat{\Theta}_{\nu\nu} \hat{a}_{\nu}^{\dagger} \hat{a}_{\nu} + \sum_{\nu=1}^2 \hbar \sqrt{V_p U_{\nu}} \hat{\Theta}_{p\nu} (\hat{a}_{\nu} + \hat{a}_{\nu}^{\dagger}) + \hbar \sqrt{U_1 U_2} \hat{\Theta}_{12} (\hat{a}_1^{\dagger} \hat{a}_2 + \hat{a}_2^{\dagger} \hat{a}_1). \quad (\text{A3})$$

The interaction is characterized by the pump lattice depth V_p and the single-particle dispersive shift $U_{\nu=1,2} = g_{\nu=1,2}^2/\Delta_a$, where g_{ν} is the vacuum Rabi frequency of cavity ν . For brevity, we defined the atomic operators

$$\hat{\Theta}_{\mu\nu} = \sum_{j=1}^N \cos(\vec{k}_{\mu} \cdot \hat{x}_j) \cos(\vec{k}_{\nu} \cdot \hat{x}_j), \quad \mu, \nu = p, 1, 2. \quad (\text{A4})$$

The cavity wavevectors \vec{k}_1 and \vec{k}_2 are for the present setup given by $\vec{k}_1 = |\vec{k}_1|(\sqrt{3}/2\vec{e}_x - 1/2\vec{e}_y)$ and $\vec{k}_2 = |\vec{k}_2|(\sqrt{3}/2\vec{e}_x + 1/2\vec{e}_y)$. For the considered cavity detunings Δ_1, Δ_2 , we can assume that the wavenumbers of the cavity modes and the pump mode are identical, that is, $|\vec{k}_p| = |\vec{k}_1| = |\vec{k}_2| \equiv k$.

2. Adiabatic elimination of the cavities

In order to simplify the theoretical description of the system, we employ the method developed in Refs. [60, 61] to adiabatically eliminate the cavities' degrees of freedom from the master equation (A1). This leads to an effective master equation, which we here report for the specific choice $\Delta_a > 0$:

$$\frac{\partial}{\partial t} \hat{\rho}_{\text{sys}} = -\frac{i}{\hbar} \left[\hat{H}_a + \frac{\hbar}{2} \sum_{\nu=1}^2 \sqrt{V_p U_\nu} \left(\hat{\alpha}_\nu^\dagger \hat{\Theta}_{p\nu} + \hat{\Theta}_{p\nu}^\dagger \hat{\alpha}_\nu \right), \hat{\rho}_{\text{sys}} \right] + \sum_{\nu=1}^2 \kappa_\nu \mathcal{L}[\hat{\alpha}_\nu] \hat{\rho}_{\text{sys}}, \quad (\text{A5})$$

describing the dynamics of the particles' external degrees of freedom, with $\hat{\rho}_{\text{sys}}$ the reduced atomic density operator. The atomic operators $\hat{\alpha}_{1,2}$ represent effective quantum fields [62]:

$$\hat{\alpha}_1 = \sqrt{V_p U_1} \frac{\hat{\Theta}_{p1} \hat{Z}_2 - U_2 \hat{\Theta}_{12} \hat{\Theta}_{p2}}{U_1 U_2 \hat{\Theta}_{12}^2 - \hat{Z}_1 \hat{Z}_2} \quad \text{and} \quad \hat{\alpha}_2 = \sqrt{V_p U_2} \frac{\hat{\Theta}_{p2} \hat{Z}_1 - U_1 \hat{\Theta}_{12} \hat{\Theta}_{p1}}{U_1 U_2 \hat{\Theta}_{12}^2 - \hat{Z}_1 \hat{Z}_2}, \quad (\text{A6})$$

where $\hat{Z}_\nu = -\Delta_\nu + U_\nu \hat{\Theta}_{\nu\nu} - i\kappa_\nu/2$, with $\nu = 1, 2$. We refer to Ref. [62, 63] for a discussion on the limits of validity.

3. Mean-field Hamiltonian

The mean-field master equation is derived using the mean-field ansatz

$$\hat{\rho}_{\text{sys}} = \otimes_{j=1}^N \hat{\rho}_a. \quad (\text{A7})$$

Integrating out the other $N - 1$ variables we obtain the (non-linear) mean-field master equation

$$\frac{\partial}{\partial t} \hat{\rho}_a = -\frac{i}{\hbar} \left[\frac{\hat{p}^2}{2m} + \hat{H}_{\text{mf}}[\hat{\rho}_a], \hat{\rho}_a \right], \quad (\text{A8})$$

describing the dynamics of the single-particle density operator $\hat{\rho}_a$. The mean-field Hamiltonian takes the form

$$\hat{H}_{\text{mf}}[\hat{\rho}_a] = \hbar V_p \hat{\theta}_p^2 + \sum_{\nu=1}^2 \hbar U_\nu |\alpha_\nu[\hat{\rho}_a]|^2 \hat{\theta}_\nu^2 + \sum_{\nu=1}^2 2\hbar \sqrt{V_p U_\nu} \text{Re}(\alpha_\nu[\hat{\rho}_a]) \hat{\theta}_p \hat{\theta}_\nu + 2\hbar \sqrt{U_1 U_2} \text{Re}(\alpha_1^*[\hat{\rho}_a] \alpha_2[\hat{\rho}_a]) \hat{\theta}_1 \hat{\theta}_2. \quad (\text{A9})$$

Here, $\hat{\theta}_\mu = \cos(\vec{k}_\mu \cdot \hat{x})$, with $\mu = p, 1, 2$, and the amplitudes of the cavity fields $\alpha_{1,2}$ have the similar form as their operator counterparts (A6) with the operators $\hat{\Theta}_{\mu\nu}$ essentially replaced by the expectation values $\langle \hat{\theta}_\mu \hat{\theta}_\nu \rangle$:

$$\alpha_1[\hat{\rho}_a] = \sqrt{V_p U_1 N} \frac{\langle \hat{\theta}_p \hat{\theta}_1 \rangle Z_2 - U_2 N \langle \hat{\theta}_p \hat{\theta}_2 \rangle \langle \hat{\theta}_1 \hat{\theta}_2 \rangle}{U_1 U_2 N^2 \langle \hat{\theta}_1 \hat{\theta}_2 \rangle^2 - Z_1 Z_2} \quad \text{and} \quad \alpha_2[\hat{\rho}_a] = \sqrt{V_p U_2 N} \frac{\langle \hat{\theta}_p \hat{\theta}_2 \rangle Z_1 - U_1 N \langle \hat{\theta}_p \hat{\theta}_1 \rangle \langle \hat{\theta}_1 \hat{\theta}_2 \rangle}{U_1 U_2 N^2 \langle \hat{\theta}_1 \hat{\theta}_2 \rangle^2 - Z_1 Z_2}, \quad (\text{A10})$$

where $Z_{\nu=1,2} = U_\nu N \langle \hat{\theta}_\nu^2 \rangle - \Delta_\nu - i\kappa_\nu/2$.

For vanishing cavity loss rates (namely, when α_ν real), the mean-field Hamiltonian (A9) can be cast in the form

$$\hat{H}_{\text{mf}}^{(\text{blue})} = \hbar \left(\sqrt{V_p} \hat{\theta}_p + \sum_{\nu=1}^2 \sqrt{U_\nu N} \alpha_\nu \hat{\theta}_\nu \right)^2, \quad (\text{A11})$$

thus showing that the mean-field energy is bounded from below, $\langle \hat{H}_{\text{mf}}^{(\text{blue})} \rangle \geq 0$. This expression is strictly valid provided that $V_p, U_{\nu=1,2}$ are positive, corresponding to an atom-pump detuning on the blue side, $\Delta_a > 0$. For red detunings, instead, these quantities are negative and the mean-field Hamiltonian can be rewritten as

$$\hat{H}_{\text{mf}}^{(\text{red})} = -\hbar \left(\sqrt{|V_p|} \hat{\theta}_p + \sum_{\nu=1}^2 \sqrt{|U_\nu| N} \alpha_\nu \hat{\theta}_\nu \right)^2. \quad (\text{A12})$$

Oppose to the previous case, the mean-field energy is here bounded from above by zero, $\langle \hat{H}_{\text{mf}}^{(\text{red})} \rangle \leq 0$.

4. Destructive interference for blue detunings

Minimization of the mean-field potential in the blue-detuned case, Eq. (A11), is achieved when $\langle \hat{H}_{\text{mf}}^{(\text{blue})} \rangle = 0$. An oversimplified argument, treating the atoms as classical scatterers and neglecting fluctuations [41], shows that this can be obtained when

$$\sqrt{V_p} \theta_p(\vec{x}) + \sum_{\nu=1}^2 \sqrt{U_\nu} \alpha_\nu \theta_\nu(\vec{x}) = 0. \quad (\text{A13})$$

Physically, this condition describes the (classical) destructive interference between the light fields of the pump and the cavities, effectively reducing the light-field potential at the positions of the particles. In order to get insight whether this condition is fulfilled by patterns that emit only into one cavity mode ("phase exclusion") or simultaneously into both cavity fields ("phase coexistence"), it is convenient to decompose their amplitudes α_1, α_2 , Eq. (A10), into the sum of the component $\alpha_\nu^{(0)}$, corresponding to the field in the absence of the coupling to the second cavity, and the amplitude $\bar{\alpha}_\nu$, which appears due to the coupling with the other cavity mode:

$$\alpha_\nu = \alpha_\nu^{(0)} + \bar{\alpha}_\nu, \quad (\text{A14})$$

with

$$\alpha_\nu^{(0)} = -\sqrt{V_p U_\nu} N \langle \hat{\theta}_\nu \hat{\theta}_p \rangle / Z_\nu \quad (\text{A15})$$

and $Z_\nu = U_\nu N (\langle \hat{\theta}_\nu^2 \rangle - 1/C_\nu)$. Here, we have also introduced a generalized definition of cooperativity of mode ν : $C_\nu = NU_\nu / (\Delta_\nu + i\kappa_\nu/2)$, such that the real (imaginary) part corresponds to the dispersive (absorptive) cooperativity apart for a sign. The contribution due to the coupling with the other mode reads

$$\bar{\alpha}_1 = \alpha_1^{(0)} \frac{u}{1-u} - \alpha_2^{(0)} \frac{\sqrt{U_1 U_2} N \langle \hat{\theta}_1 \hat{\theta}_2 \rangle}{Z_1} \frac{1}{1-u}, \quad (\text{A16})$$

with $u = U_1 U_2 N^2 \langle \hat{\theta}_1 \hat{\theta}_2 \rangle^2 / (Z_1 Z_2)$ and $\bar{\alpha}_2$ is found by swapping the subscripts $1 \leftrightarrow 2$ in the above expression. In the absence of cross-coupling between the two cavity modes, the amplitude of cavity field ν is directly proportional to the expectation value $\langle \hat{\theta}_\nu \hat{\theta}_\nu \rangle$. In the presence of the cross coupling, $\bar{\alpha}_\nu \neq 0$, the amplitude also depends on the order parameter of the other cavity. The effect of the cross coupling is two-fold: As visible from Eq. (A16), a finite field in one resonator can seed a field in the other mode. However, in the blue, the formation of the second field tends to deplete the first, as such, the cross-coupling tends to inhibit the occupation of the second cavity. For sufficiently low pump-lattice depths V_p , the condition (A13) can be fulfilled by employing the field of a single cavity. Above a critical pump-lattice depth V_p^* , however, the contribution of the pump field dominates over the field of the occupied cavity. At this point, the build-up of the second cavity field is required to maintain the destructive interference. This gives rise to the threshold for coexistence reported in Fig. 2, see Ref. [61] for details.

5. Gross-Pitaevskii and Generalized Gross-Pitaevskii equation

The Gross-Pitaevskii equation with (GPE) given in the main text, Eq. (1), is derived from Eq. (A9) after writing the mean-field Hamiltonian in second quantization, adding the trapping potential and the van-der-Waals scattering term, and making the ansatz of symmetry breaking. The generalized Gross-Pitaevskii equation (GGPE) follows directly from the GPE by neglecting the trapping potential, $\omega_{\nu=x,y} = 0$, and the short-range interaction, $V_0 = 0$, and reads explicitly

$$i\hbar \frac{\partial}{\partial t} \psi(\vec{x}, t) = \left(-\frac{\hbar^2 \vec{\nabla}^2}{2m} + H_{\text{mf}}[\psi] \right) \psi(\vec{x}, t). \quad (\text{A17})$$

The mean-field Hamiltonian \hat{H}_{mf} is identical to Eq. (A9), where the expectation values in the cavity amplitudes, Eq. (A10), are now taken over the wavefunction ψ , $\langle \hat{\theta}_p \hat{\theta}_c \rangle = \int d\vec{x} \psi^*(\vec{x}, t) \theta_p(\vec{x}) \theta_c(\vec{x}) \psi(\vec{x}, t)$.

6. Numerical Simulations

In this section, we give further details on the numerical simulations we performed based on the GPE.

a. *Implementation*

The GPE has been implemented numerically using the Julia package `QuantumOptic.jl`[64]. The wavefunction $\psi(\vec{x}, t)$ is here discretized in space over a two-dimensional grid with $n_x \times n_y$ points and spanning the range $[-L_x/2, L_x/2] \times [-L_y/2, L_y/2]$. The lengths $L_{x,y}$ are fixed by the extension of the atomic cloud, which can be estimated by the spatial extension of a trapped two-dimensional BEC in its ground state. In the Thomas-Fermi limit, the ground-state density is close to the Thomas-Fermi solution $|\psi_{\text{TF}}|^2$, found by solving the GPE (1) for its steady state when neglecting the mean-field potential \hat{H}_{mf} and the kinetic energy term:

$$|\psi_{\text{TF}}(x, y)|^2 = \frac{2}{\pi R_x R_y} \begin{cases} 1 - \left(\frac{x}{R_x}\right)^2 - \left(\frac{y}{R_y}\right)^2, & (x/R_x)^2 + (y/R_y)^2 \leq 1 \\ 0, & \text{otherwise.} \end{cases} \quad (\text{A18})$$

The size of the cloud is characterized by the Thomas-Fermi radii

$$R_\nu = \frac{1}{\omega_\nu} \left(\frac{4}{m\pi} V_0 N \omega_x \omega_y \right)^{\frac{1}{4}}, \quad \nu = x, y. \quad (\text{A19})$$

Typical grid sizes $L_{x,y}$ are chosen between 1.4 – 1.6 times the Thomas-Fermi radii. While the extension of the cloud is mainly dictated by the short-range interaction and the harmonic trapping potential, the step sizes dx and dy are controlled by the light fields of the pump and the cavities, in particular, the periodic potentials they create. In the simulations, we choose the stepsizes to fit 8 – 12 grid points within one wavelength $\lambda = 2\pi/k$ to resolve these structures. For the experimental parameters, this leads to typical grid sizes $n_{x,y}$ with 300 - 400 points per spatial direction.

b. *Contact-interaction potential*

In three dimensions, the contact interaction is given by $V_0^{(3D)} = 4\pi\hbar^2 a_s/m$. For Rubidium 87, the mass is $m = 1.44316 \times 10^{-25}$ kg [59] and the scattering length is $a_s = 98a_0$, with a_0 the Bohr radius. In three dimensions, the Thomas-Fermi radii can be derived similar to the preceding paragraph, leading to

$$R_\nu^{(3D)} = \frac{1}{\omega_\nu} \left(\frac{15}{4\pi} \frac{V_0^{(3D)} N \omega_x \omega_y \omega_z}{m} \right)^{\frac{1}{5}}. \quad (\text{A20})$$

The two-dimensional contact interaction strength V_0 in our GPE simulations is chosen so that the extension of the cloud in the x - y -plane matches the one of a three-dimensional cloud. Thus, by requiring that $R_{x,y}^{(3D)} = R_{x,y}$, we find the following expression for the two-dimensional contact interaction strength

$$V_0 = \left(\frac{15^4 \pi}{2^{18}} \frac{m \omega_z^4}{\omega_x \omega_y} \frac{(V_0^{(3D)})^4}{N} \right)^{\frac{1}{5}}. \quad (\text{A21})$$

c. *Normalization and atom losses*

The condensate wavefunction ψ is here defined such that the normalization $\mathcal{P} = \int_{\mathbb{R}^2} d\vec{x} |\varphi(\vec{x})|^2 = 1$ is independent of the number of particles N , as such, N appears explicitly in the GPE (1) via the short- and long-range interaction (see, for instance, Eq. (A10)). When solving the GPE for the dynamics of the system, we account for the atom losses of the experiment. This is done by adding to the GPE a phenomenological loss term $-i\Gamma/2\psi$, leading to an exponential decay of the initially normalized wavefunction over time with rate Γ , such that $\mathcal{P}(t) = e^{-\Gamma t}$. As extracted from the characterization of the experiment (see Appendix C), we estimate the loss rate Γ to range between 2 and 4 Hz. In the presence of atom losses, N represents in the dynamical equation the initial number of atoms in the BEC, while the number of atoms at time t is given by $N\mathcal{P}(t)$. It is important to note that the contact interaction strength (A21) has to be replaced by $V_0 e^{\Gamma t/5}$ to ensure the correct size of the cloud in the x - y -plane (See Sec. A 6 b) at any time t .

Appendix B: Linear Stability Analysis

In this Section, we present the details of the linear stability analysis, the tool that is used in Fig. 4 to make predictions about the subradiant states' lifetime.

1. Derivation

We start by deriving the equations that are at the basis of the linear stability analysis from the mean-field master equation (A8). Let $\hat{\rho}_{\text{ss}}$ be a generic steady state of this equation, thus fulfilling

$$\left[\frac{\hat{p}^2}{2m} + \hat{H}_{\text{mf}}[\hat{\rho}_{\text{ss}}], \hat{\rho}_{\text{ss}} \right] = 0. \quad (\text{B1})$$

We define the deviation from this state $\delta\hat{\rho}_a(t) = \hat{\rho}_a(t) - \hat{\rho}_{\text{ss}}$, obeying the equation of motion

$$\frac{\partial}{\partial t} \delta\hat{\rho}_a = -\frac{i}{\hbar} \left[\frac{\hat{p}^2}{2m} + \hat{H}_{\text{mf}}[\hat{\rho}_{\text{ss}} + \delta\hat{\rho}_a(t)], \hat{\rho}_{\text{ss}} + \delta\hat{\rho}_a(t) \right], \quad (\text{B2})$$

which we linearize in the following. For this purpose, we first expand the cavity amplitudes $\alpha_\nu[\hat{\rho}_{\text{ss}} + \delta\hat{\rho}_a]$ to first order in the expectation values' fluctuations $\delta\langle\hat{\theta}_\mu\hat{\theta}_\nu\rangle = \text{Tr}\{\hat{\theta}_\mu\hat{\theta}_\nu\delta\hat{\rho}_a\}$. For the amplitude of cavity 1, we find

$$\alpha_1[\hat{\rho}_{\text{ss}} + \delta\hat{\rho}_a] = \alpha_1[\hat{\rho}_{\text{ss}}] + a_{1,11}[\hat{\rho}_{\text{ss}}]\delta\langle\hat{\theta}_1^2\rangle + a_{1,22}[\hat{\rho}_{\text{ss}}]\delta\langle\hat{\theta}_2^2\rangle + a_{1,p1}[\hat{\rho}_{\text{ss}}]\delta\langle\hat{\theta}_p\hat{\theta}_1\rangle + a_{1,p2}[\hat{\rho}_{\text{ss}}]\delta\langle\hat{\theta}_p\hat{\theta}_2\rangle + a_{1,12}[\hat{\rho}_{\text{ss}}]\delta\langle\hat{\theta}_1\hat{\theta}_2\rangle. \quad (\text{B3})$$

The coefficients a depend on the specific steady state $\hat{\rho}_{\text{ss}}$ we consider and are explicitly given by

$$\begin{aligned} a_{1,11}[\hat{\rho}_{\text{ss}}] &= \frac{U_1 N Z_{2,\text{ss}}}{U_1 U_2 N^2 \langle\hat{\theta}_1\hat{\theta}_2\rangle_{\text{ss}}^2 - Z_{1,\text{ss}} Z_{2,\text{ss}}} \alpha_1[\hat{\rho}_{\text{ss}}], & a_{1,22}[\hat{\rho}_{\text{ss}}] &= \frac{U_2 N \left(\sqrt{V_p U_1} N \langle\hat{\theta}_p\hat{\theta}_1\rangle_{\text{ss}} + Z_{1,\text{ss}} \alpha_1[\hat{\rho}_{\text{ss}}] \right)}{U_1 U_2 N^2 \langle\hat{\theta}_1\hat{\theta}_2\rangle_{\text{ss}}^2 - Z_{1,\text{ss}} Z_{2,\text{ss}}}, \\ a_{1,p1}[\hat{\rho}_{\text{ss}}] &= \frac{\sqrt{V_p U_1} N Z_{2,\text{ss}}}{U_1 U_2 N^2 \langle\hat{\theta}_1\hat{\theta}_2\rangle_{\text{ss}}^2 - Z_{1,\text{ss}} Z_{2,\text{ss}}}, & a_{1,p2}[\hat{\rho}_{\text{ss}}] &= -\frac{U_2 N \sqrt{V_p U_1} N \langle\hat{\theta}_1\hat{\theta}_2\rangle_{\text{ss}}}{U_1 U_2 N^2 \langle\hat{\theta}_1\hat{\theta}_2\rangle_{\text{ss}}^2 - Z_{1,\text{ss}} Z_{2,\text{ss}}}, \\ a_{1,12}[\hat{\rho}_{\text{ss}}] &= -\frac{U_2 N \left(\sqrt{V_p U_1} N \langle\hat{\theta}_p\hat{\theta}_2\rangle_{\text{ss}} + 2U_1 N \langle\hat{\theta}_1\hat{\theta}_2\rangle_{\text{ss}} \alpha_1[\hat{\rho}_{\text{ss}}] \right)}{U_1 U_2 N^2 \langle\hat{\theta}_1\hat{\theta}_2\rangle_{\text{ss}}^2 - Z_{1,\text{ss}} Z_{2,\text{ss}}}, \end{aligned} \quad (\text{B4})$$

where $\langle\hat{\theta}_\mu\hat{\theta}_\nu\rangle_{\text{ss}} = \text{Tr}\{\hat{\theta}_\mu\hat{\theta}_\nu\hat{\rho}_{\text{ss}}\}$ and $Z_{\nu,\text{ss}} = U_\nu N \langle\hat{\theta}_\nu^2\rangle_{\text{ss}} - \Delta_\nu - i\kappa_\nu/2$. The expansion for the cavity 2 amplitude α_2 can be directly obtained from Eq. (B3) by interchanging all subscripts 1 and 2. Plugging these expansions in the mean-field Hamiltonian $\hat{H}_{\text{mf}}[\hat{\rho}_{\text{ss}} + \delta\hat{\rho}_a]$ and neglecting consistently terms that are of second or higher order in the fluctuations $\delta\langle\hat{\theta}_\mu\hat{\theta}_\nu\rangle$, we find the first-order expansion

$$\hat{H}_{\text{mf}}[\hat{\rho}_{\text{ss}} + \delta\hat{\rho}_a] = \hat{H}_{\text{mf}}[\hat{\rho}_{\text{ss}}] + \hbar \sum_{(\mu,\nu) \in \mathcal{S}} \sum_{(n,m) \in \mathcal{S}} h_{nm,\mu\nu}[\hat{\rho}_{\text{ss}}] \delta\langle\hat{\theta}_\mu\hat{\theta}_\nu\rangle \hat{\theta}_n \hat{\theta}_m. \quad (\text{B5})$$

For brevity, we introduced the set $\mathcal{S} = \{(1,1), (2,2), (p,1), (p,2), (1,2)\}$ of possible index tuple and the coefficients h are given by

$$\begin{aligned} h_{11,\mu\nu}[\hat{\rho}_{\text{ss}}] &= 2U_1 \text{Re} \{ a_{1,\mu\nu} (\alpha_1[\hat{\rho}_{\text{ss}}])^* \}, & h_{22,\mu\nu}[\hat{\rho}_{\text{ss}}] &= 2U_2 \text{Re} \{ a_{2,\mu\nu} (\alpha_2[\hat{\rho}_{\text{ss}}])^* \}, \\ h_{p1,\mu\nu}[\hat{\rho}_{\text{ss}}] &= 2\sqrt{V_p U_1} \text{Re} \{ a_{1,\mu\nu} \}, & h_{p2,\mu\nu}[\hat{\rho}_{\text{ss}}] &= 2\sqrt{V_p U_2} \text{Re} \{ a_{2,\mu\nu} \}, \\ h_{12,\mu\nu}[\hat{\rho}_{\text{ss}}] &= 2\sqrt{U_1 U_2} \text{Re} \{ (a_{1,\mu\nu})^* \alpha_2[\hat{\rho}_{\text{ss}}] + (\alpha_1[\hat{\rho}_{\text{ss}}])^* a_{2,\mu\nu} \}. \end{aligned} \quad (\text{B6})$$

With the expansion (B5), the linearized equation of motion (B2) is found to be

$$\frac{\partial}{\partial t} \delta\hat{\rho}_a = \mathcal{L}_0 \delta\hat{\rho}_a - i \sum_{(\mu,\nu) \in \mathcal{S}} \sum_{(n,m) \in \mathcal{S}} h_{nm,\mu\nu}[\hat{\rho}_{\text{ss}}] \left[\hat{\theta}_n \hat{\theta}_m, \hat{\rho}_{\text{ss}} \right] \delta\langle\hat{\theta}_\mu\hat{\theta}_\nu\rangle, \quad (\text{B7})$$

where we introduced for later convenience

$$\mathcal{L}_0 \delta \hat{\rho}_a = -\frac{i}{\hbar} \left[\frac{\hat{p}^2}{2m} + \hat{H}_{\text{mf}}[\hat{\rho}_{\text{ss}}], \delta \hat{\rho}_a \right]. \quad (\text{B8})$$

The objective of this analysis is to determine whether a small but finite deviation $\delta \hat{\rho}_a$ is amplified or damped by the system, thus, signaling the instability or stability of the steady state $\hat{\rho}_{\text{ss}}$, respectively. For this purpose, we can avoid explicitly solving the linearized equation of motion (B7) and study the spectrum of the superoperator on the right-hand side instead, following the steps outlined in Ref. [65]. Applying the Laplace transform L , formally defined as

$$L[f](s) = \int_0^\infty dt e^{-st} f(t), \quad s \in \mathbb{C}, \quad (\text{B9})$$

to the linearized equation, we obtain

$$sL[\delta \hat{\rho}_a](s) - \delta \hat{\rho}_a(t=0) = \mathcal{L}_0 L[\delta \hat{\rho}_a](s) - i \sum_{(\mu,\nu) \in \mathcal{S}} \sum_{(n,m) \in \mathcal{S}} h_{nm,\mu\nu}[\hat{\rho}_{\text{ss}}] \left[\hat{\theta}_n \hat{\theta}_m, \hat{\rho}_{\text{ss}} \right] L[\delta \langle \hat{\theta}_\mu \hat{\theta}_\nu \rangle](s). \quad (\text{B10})$$

Solving this equation formally for $L[\delta \hat{\rho}_a](s)$ leads to

$$L[\delta \hat{\rho}_a](s) = (s - \mathcal{L}_0)^{-1} \delta \hat{\rho}_a(t=0) - i \sum_{(\mu,\nu) \in \mathcal{S}} \sum_{(n,m) \in \mathcal{S}} h_{nm,\mu\nu}[\hat{\rho}_{\text{ss}}] (s - \mathcal{L}_0)^{-1} \left[\hat{\theta}_n \hat{\theta}_m, \hat{\rho}_{\text{ss}} \right] L[\delta \langle \hat{\theta}_\mu \hat{\theta}_\nu \rangle](s). \quad (\text{B11})$$

Multiplying this equation from the left by $\hat{\theta}_\alpha \hat{\theta}_\beta$ and taking the trace, we get

$$L[\delta \langle \hat{\theta}_\alpha \hat{\theta}_\beta \rangle](s) = b_{\alpha\beta}(s) - \sum_{(\mu,\nu) \in \mathcal{S}} \sum_{(n,m) \in \mathcal{S}} C_{\alpha\beta,nm} h_{nm,\mu\nu} L[\delta \langle \hat{\theta}_\mu \hat{\theta}_\nu \rangle](s), \quad (\text{B12})$$

where $b_{\alpha\beta} = \text{Tr}\{\hat{\theta}_\alpha \hat{\theta}_\beta (s - \mathcal{L}_0)^{-1} \delta \hat{\rho}_a(t=0)\}$ and $C_{\alpha\beta,nm} = i \text{Tr}\{\hat{\theta}_\alpha \hat{\theta}_\beta (s - \mathcal{L}_0)^{-1} [\hat{\theta}_n \hat{\theta}_m, \hat{\rho}_{\text{ss}}]\}$. Here, we also used the fact that the trace and the Laplace transform are commuting operations, such that $\text{Tr}\{\hat{\theta}_\alpha \hat{\theta}_\beta L[\delta \hat{\rho}_a](s)\} = L[\delta \langle \hat{\theta}_\alpha \hat{\theta}_\beta \rangle](s)$. Equation (B12) represents a set of five coupled equations for the Laplace transformed fluctuations in the observables $L[\delta \langle \hat{\theta}_\alpha \hat{\theta}_\beta \rangle](s)$. In fact, introducing the vector $\vec{Y}(s) = (L[\delta \langle \hat{\theta}_1^2 \rangle](s), L[\delta \langle \hat{\theta}_2^2 \rangle](s), L[\delta \langle \hat{\theta}_p \hat{\theta}_1 \rangle](s), L[\delta \langle \hat{\theta}_p \hat{\theta}_2 \rangle](s), L[\delta \langle \hat{\theta}_1 \hat{\theta}_2 \rangle](s))^T$, we can combine all five equations in a single matrix-vector equation

$$\vec{Y}(s) = \vec{b}(s) - \mathcal{C}(s) \mathcal{H} \vec{Y}(s), \quad (\text{B13})$$

where the entries of the 5×5 matrices \mathcal{C} and \mathcal{H} follow directly from Eq (B12). The formal solution of this equation reads

$$\vec{Y}(s) = (1 + \mathcal{C}(s) \mathcal{H})^{-1} \vec{b}(s). \quad (\text{B14})$$

The poles s^* of the right-hand side determine the short-time behaviour of the fluctuations $\delta \langle \hat{\theta}_\mu \hat{\theta}_\nu \rangle$, with the pole s^* that has the largest real part $\gamma = \text{Re}\{s^*\}$ giving the main contribution. Specifically, if $\gamma > 0$, the initial fluctuation is amplified by the system, leading to an exponential growth of the fluctuations with rate γ , $\delta \langle \hat{\theta}_\mu \hat{\theta}_\nu \rangle \sim e^{\gamma t}$, and signaling the instability of the considered steady-state $\hat{\rho}_{\text{ss}}$. In the main text and hereafter, we refer to this rate $\gamma > 0$ as escape rate. If instead $\gamma \leq 0$, the initial fluctuation is damped and we consider the steady state to be stable. The poles s^* are the roots of the dispersion relation

$$\det(1 + \mathcal{C}(s) \mathcal{H}) = 0. \quad (\text{B15})$$

Given the complexity of this equation, we resort to numerical methods to determine the roots.

2. Prediction of the subradiant state's lifetime

The subradiant state represents a stable solution of the mean-field master equation (A8). As such, we can employ the linear stability analysis of the preceding section to determine its stability for given parameters. As we will discuss in the following, this allows us to predict its lifetime in the presence of atom losses.

In Fig. 4, we study quenches from cavity 2 to 1. Here, the subradiant state of the system (after performing the quench) is characterized by a spatial configuration that supports the scattering of photons into cavity 2 but suppresses scattering into cavity 1. The corresponding steady state $\hat{\rho}_{\text{sub}}$ can be computed by solving the steady-state condition (B1) for the cavity detunings after the quench, $(\Delta_1, \Delta_2) = (0, \delta)$, and for vanishing coupling to cavity 1, $g_1 = 0$. We verify that this state obeys our definition of the subradiant state, that is, $\text{Tr}\{\hat{\theta}_p \hat{\theta}_1 \hat{\rho}_{\text{sub}}\} = \text{Tr}\{\hat{\theta}_1 \hat{\theta}_2 \hat{\rho}_{\text{sub}}\} = 0$. Hence, even if the coupling to cavity 1 is present, $g_1 \neq 0$, the spatial configuration prohibits the occupation of this cavity, such that $\alpha_1[\hat{\rho}_{\text{sub}}] = 0$, and the state $\hat{\rho}_{\text{sub}}$ remains a steady state of the dynamical equation. By numerically computing the roots of the dispersion relation (B15) for the state $\hat{\rho}_{\text{ss}} = \hat{\rho}_{\text{sub}}$ and for $g_1 \neq 0$, we determine its stability. A root with positive real part $\gamma > 0$ indicates that the coupling to cavity 1 renders the subradiant state unstable, otherwise it remains stable. Repeating this calculation for different quench strengths δ and atom numbers N , we construct the stability diagram reported in Fig. 4 b).

As visible from this stability diagram, we can identify for each considered quench strength δ a critical atom number $N_c(\delta)$ below which the subradiant state becomes unstable ($\gamma > 0$). Suppose that the atom number after the quench is N_0 , ranging between 2.43×10^5 and 2.97×10^5 , then the subradiant state represents a stable configuration if $N_0 > N_c$. Even if initially fulfilled, atom losses eventually decrease the atom number over time, $N(t) \leq N_0$, and the subradiant state becomes unstable when $N(t^*) = N_c$. Thus, the atom loss brings the system from the stable region ($\gamma \leq 0$) to the unstable region ($\gamma > 0$) in the stability diagram, as indicated by the green arrow in Fig. 4 b). The delay times shown in Fig. 4 a) represent essentially the length of the time interval it takes the atom losses to decrease the initial atom number below the critical value. Imposing as above an exponential decay of the atom number, $N(t) = N_0 e^{-\Gamma t}$, we can predict the delay time t^* by solving the condition $N e^{-\Gamma t^*} = N_c$, yielding

$$t^*(\delta) = -\frac{1}{\Gamma} \ln \left(\frac{N_c(\delta)}{N_0} \right). \quad (\text{B16})$$

It is important to note that this equation only allows us to make viable predictions about the delay time if the system state $\hat{\rho}_a(t)$ remains close to the subradiant state $\hat{\rho}_{\text{sub}}$ after the quench. In particular, as the latter is a function of the atom number, $\hat{\rho}_{\text{sub}} = \hat{\rho}_{\text{sub}}(N)$, the subradiant state changes over time when atom losses are present. However, as the atom losses occur on a much longer timescale than the one associated with the long-range interaction, the system - if initially trapped in the subradiant state - is able to follow adiabatically the subradiant state.

Appendix C: Experimental Details

Preparation of the Bose Einstein condensate (BEC) and balancing the two atom-cavity couplings

Our experimental protocol starts with the preparation of a ^{87}Rb Bose-Einstein condensate (BEC) of $N = 2.7(3) \times 10^5$ and $T = 102(10)$ nK via optical evaporation. An optical dipole trap with trapping frequencies $[\omega_x, \omega_y, \omega_z] = 2\pi \times [106(1), 71.2(3), 223(3)]$ Hz positions the BEC at the crossing point of the two cavity modes.

The atom-cavity coupling is proportional to the overlap of the cavity mode with the atom cloud, and can be measured via the dispersive shift of the cavity resonance. Moving the trap to different locations and measuring the dispersive shift as a function of the trap position allows us to map out the effective coupling strengths for both resonators. Since the cavity mode centers differ by $12 \mu\text{m}$ in height, where the mode waist radius is $50 \mu\text{m}$, we can adjust the trap position such that the coupling to both resonators is balanced. Slight misalignments can however lead to a systematic shift of the phase boundary between the two ordered phases. The data in Figure 2 has therefore been shifted by 0.1 MHz to compensate for this systematic error.

A magnetic offset field of ~ 25 G is applied to avoid spin-dependent effects on self-organization as e.g. superradiance to the orthogonally polarized cavity mode that is significantly detuned due to the birefringence of our cavity as we studied in [66].

Cavities and phase diagrams

The cavity modes are tilted at an angle of 60° and have distinct decay rates $[\kappa_1, \kappa_2] = 2\pi \times [147(4), 800(11)]$ kHz. The maximum single-atom vacuum Rabi frequencies of $[g_1, g_2] = 2\pi \times [1.95(1), 1.77(1)]$ MHz are comparable for both cavities. At a 60° angle relative to each cavity, a retroreflected pump beam creates a standing wave lattice. We refer to this beam as the transverse pump. Its frequency ω_p is blue detuned by $\Delta_a = \omega_p - \omega_a = 2\pi \times 69.8(1)$ GHz with respect to ω_a , the D₂-line of ^{87}Rb . We further introduce the relative detunings $\Delta_\nu = \omega_p - \omega_\nu$ (with $\nu \in \{1, 2\}$) of the cavity resonance frequencies ω_ν and the transverse pump. These detunings between the frequency of the transverse

beams and the cavities are tuneable within tens of MHz via an electro-optical modulator. The lengths of the cavities are stabilized using low amplitude, far-detuned additional laser fields at 830 nm, allowing a constant feedback on the cavity lengths while having a negligible effect on the atomic cloud.

During each experimental sequence, we linearly increase the transverse pumping lattice depth V_p in 10 ms from 0 to a maximum of $10.8 E_{\text{rec}}$, in units of recoil energy, $E_{\text{rec}} = 2\pi\hbar \times 3.77 \text{ kHz}$. Meanwhile, we collect the leaking photons from each cavity and use the photon detection rates to deduce the intracavity photon numbers. Beyond a critical pump strength and for certain cavity detunings, the intracavity field is populated as the atoms self-organise into minima of the resulting lattice potential. For each cavity we repeat the transverse pumping ramp for different cavity detunings and obtain the single cavity phase diagrams as shown in Figure 5a, d. The respective other cavity is not influencing this measurement since we put it to a sufficiently large detuning. The atom-cavity couplings are well balanced for both cavities, resulting in similar phase boundaries for self-organisation. We further extend the individual phase diagrams to two cavities simultaneously close to resonance. By increasing the transverse pump power, we study the self-organisation for different detunings of cavity 1 and 2 at a fixed transverse pump lattice strength of $5.1 E_r$. We plot the photon numbers in cavity 1 (2) in Figure 5 b (e) for the given pair of cavity detunings. If the cavity field in cavity 1 (2) is larger than a defined photon number threshold, n_1^{th} (n_2^{th}), we characterise the system as self-organised in cavity 1 (2) and plot a blue (red) square in the binarized Figure 5c for the given pair of cavity detunings. A white square indicates photon levels in both cavities below the thresholds, and a grey square indicates photon levels in both cavities above the thresholds. Self-organisation occurs in the cavity closer to resonance. To further highlight this dependence, we switch to a rotated coordinate system and define the relative detuning $\Delta_1 - \Delta_2$ and the mean detuning $(\Delta_1 + \Delta_2)/2$ as the x and y axes, see Figure 5f.

Heterodyne measurement

The amplitudes of the intracavity fields are recorded using balanced optical heterodyne detectors. For each cavity, a local oscillator (LO) laser field is combined at a beam splitter with the light field leaking from a cavity mirror and directed together onto the two photodiodes of a balanced photodetector. The signal is then mixed down to a moderate radio frequency of 300 kHz using a homemade IQ filter device. The LO is generated by shifting the frequency of the same laser source as the transverse pump by 50 MHz with an acousto-optic modulator. To compensate for phase drifts introduced by sending the light fields through separate optical fibres, we lock their relative phase after passing through the fibres. For each cavity signal, the 300 kHz data is recorded using a computer connected oscilloscope (PicoScope 5444b). The signal is then processed by software which extracts the photon level and applies a low pass filter using a binning window of 1×10^{-4} s. All associated radio frequency signal sources are phase-locked to a 10 MHz GPS frequency standard which has a fractional stability better than 10^{-12} to minimise the technical phase noise in the heterodyne detection system. Further technical details and design considerations are described in detail in [67]. To calibrate the amplitude of the intracavity light field, we perform Raman-Nath diffraction analogous to the transverse pump calibration by applying a short coherent on-axis probe to the cavity.

Imaging of the atomic cloud

We use resonance absorption imaging of the atomic cloud in addition to the detection of the light field leaking from the cavities. From absorption images taken after 20 ms of ballistic expansion of the atomic cloud, the temperature, number of atoms and momentum state populations are extracted.

Atomic loss rate

We measure the loss rate of the system by preparing the cloud in the crossed beam dipole trap and ramping up the transverse pump lattice. We let the system evolve for a certain hold time before we switch off all potentials and measure the remaining atom number after ballistic expansion. Typical decay curves are shown in Figure 6 for different parameters.

Measurement protocol of the subradiant states

In the section "Lifetime of Subradiant States" in the main text, we present a measurement protocol which extracts a hysteresis region of subradiant states. For certain cavity 1 and 2 detunings, we linearly ramp up the transverse

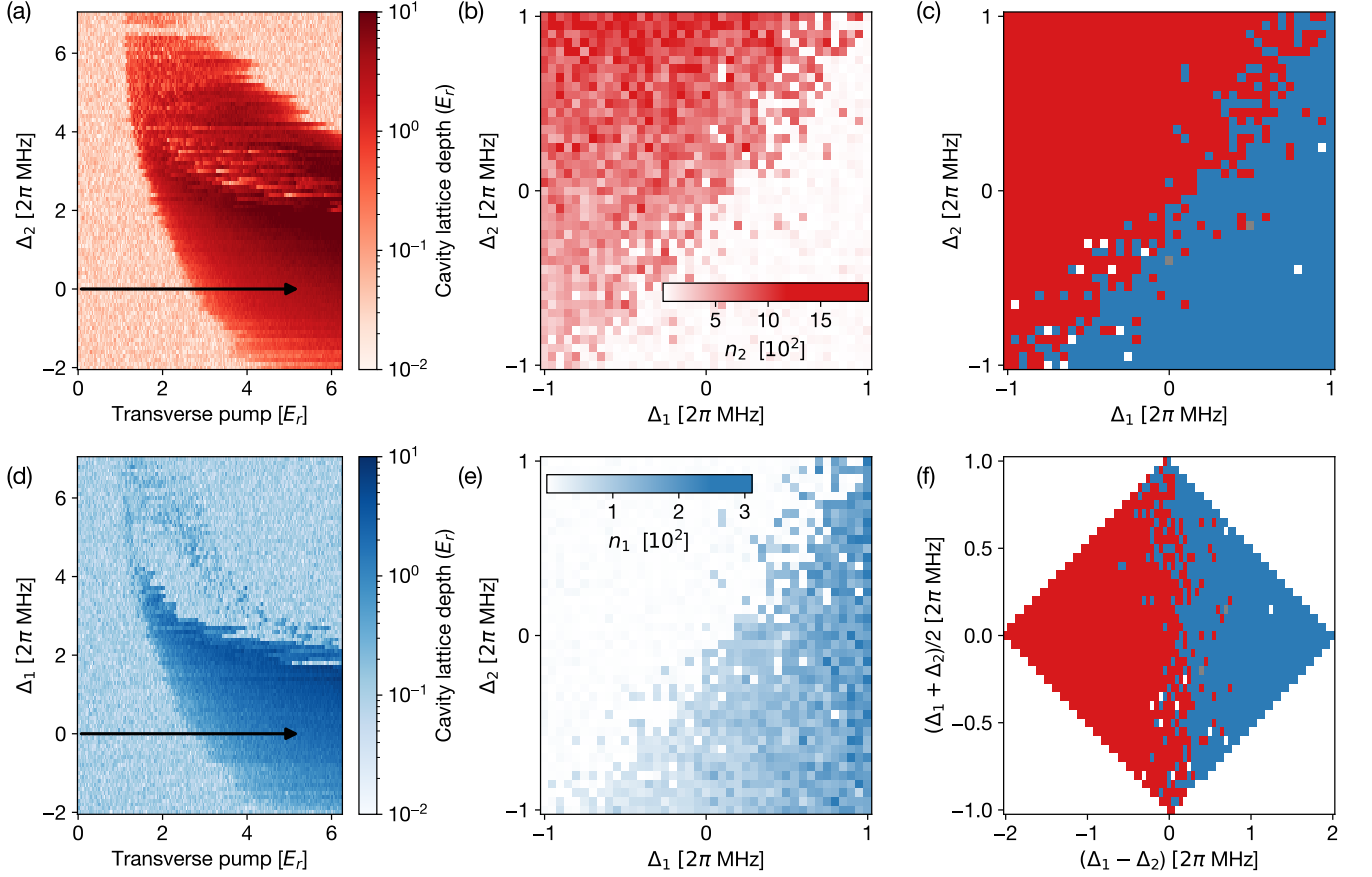


FIG. 5. Measuring Phase Diagrams. (a,d) Single cavity phase diagrams for cavity 2 (1). We linearly ramp up the transverse pump to $6.2 E_r$ and record the cavity lattice depth for different detunings Δ_2 (Δ_1). For these measurements, cavity 1 (2) is detuned far away from resonance and does not influence the self-organisation of cavity 2 (1). Black arrows highlight transverse pump ramps, where we stop the ramp at $5.1 E_r$ and collect data for the subsequent panels. (b,e) Measured intracavity photon number $n_{1(2)}$ after increasing V_p linearly from 0 to $5.1 E_r$ at fixed detunings $\Delta_{1(2)}$ (c) Combined and binarized phase diagram derived from panels (b,e) by defining thresholds of $(n_1^{\text{th}}, n_2^{\text{th}}) = (30, 200)$ photons for identifying superradiance in a respective cavity. The steady-state photon numbers, and thus defined threshold values, differ due to the different cavity decay rates. Blue (red) pixels indicate superradiance in cavity 1 (2), white pixels indicate both cavity populations are above the respective threshold, grey pixels indicate coexistence where both cavity populations are above the respective threshold. (f) Same data as in panel (c), but in rotated coordinates of relative cavity detunings $\Delta_1 - \Delta_2$ and mean cavity detunings $(\Delta_1 + \Delta_2)/2$ as used in the main text. White spaces outside the square indicate no data.

pump power in 5 ms such that the atoms self-organize into the initial cavity. Next, over 25 ms, the cavity detunings are swept across the phase boundary. The sweep is symmetric with regards to the phase boundary: one of the ramps linearly changes $\Delta_{1,2}$ from $[0.5, -0.5], 2\pi \times \text{MHz}$ to $[-0.5, 0.5], 2\pi \times \text{MHz}$ and yields $\Delta_1 - \Delta_2$ as a unique parameter characterizing this sweep. At the sweep half-time of 12.5 ms, the cavity detunings are degenerate $\Delta_1 - \Delta_2 = 0$. We extract the switching time from traces as shown in Figure 3a, which corresponds to a unique value of $\Delta_1 - \Delta_2$. We repeat this measurement for different values of $(\Delta_1 + \Delta_2)/2$ and show the results in Figure 3b.

In the section "Lifetime of Subradiant States" in the main text, we characterize the lifetimes of the subradiant system by quenching across the phase boundary between the two cavities and determining the time after which the system switches between the two cavities (see Figure 4). At the start of each quench measurement, a 10 ms long transverse pump ramp is used to prepare a self-organized state in one of the cavities. The detunings of the cavities determine which cavity gets populated. When quenching from cavity 2 to 1, cavity 2 is initially resonant with respect to the transverse pump, so $\Delta_2 = 0$ and cavity 1 is detuned to $\Delta_1 = [-0.6, -0.1] 2\pi \times \text{MHz}$. After the transverse pump ramp, we hold the final pumping strengths and cavity 1 is quenched onto resonance $\Delta_1 = 0$ and cavity 2 away from resonance by $\Delta_2 = [-0.6, -0.1] 2\pi \times \text{MHz}$. Typical photon traces for both cavities are shown in Figure 4c,e. Following a buildup of the photon level in cavity 2, the system stays self-organized in cavity 2 beyond the quench. It remains subradiant until a characteristic delay time, when the self-organization jumps from the second to the first

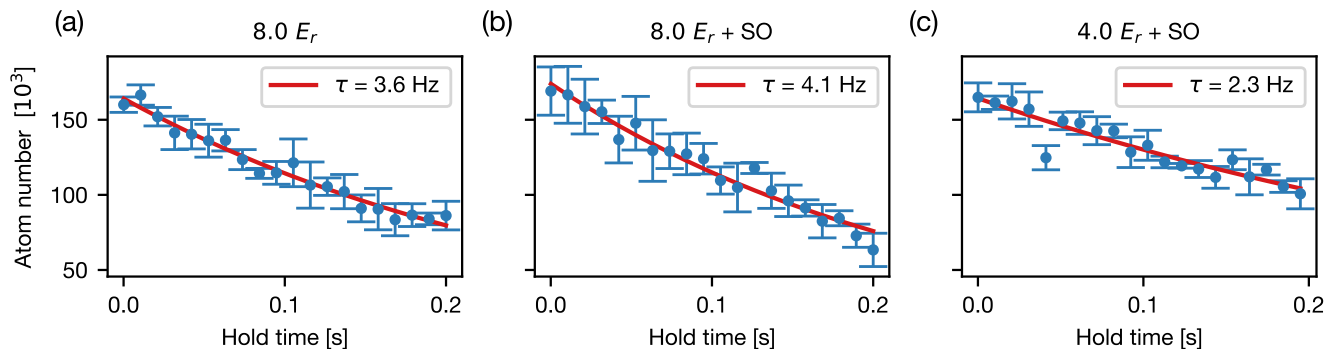


FIG. 6. **Atom loss.** The transverse pump drive is linearly ramped up in 10 ms from 0.0 to $8.0 E_r$ for (a,b) and from 0 to $4.0 E_r$ for (c). After variable hold time, the atom numbers are extracted from time-of-flight images of the cloud. The cavity 1 detuning in (a) is detuned away from resonance and atoms do not self-organise. For (b,c), the cavity 1 detuning is set to resonance such that atoms self-order during the transverse pump ramp. In all measurements cavity 2 is far detuned from resonance. This figure estimates atom loss rates of up to 4 Hz present in our experiment, which have been taken into account in the numerical models

cavity. We extract this delay time from numerically fitting a delta function in cavity 2 to the decay and in cavity 1 to the onset of the photon field. We find that both times lay within 0.1 ms. We nevertheless take the average of both as the delay time plotted in Figure 4a.

-
- [1] T. Brandes, Coherent and collective quantum optical effects in mesoscopic systems, *Physics Reports* **408**, 315 (2005).
 - [2] M. Reitz, C. Sommer, and C. Genes, Cooperative quantum phenomena in light-matter platforms, *PRX Quantum* **3**, 010201 (2022).
 - [3] R. H. Dicke, Coherence in Spontaneous Radiation Processes, *Physical Review* **93**, 99 (1954).
 - [4] M. Gross and S. Haroche, Superradiance: An essay on the theory of collective spontaneous emission, *Physics Reports* **93**, 301 (1982).
 - [5] A. Crubellier, S. Liberman, D. Pavolini, and P. Pillet, Superradiance and subradiance: I. interatomic interference and symmetry properties in three-level systems, *Journal of Physics B: Atomic and Molecular Physics J. Phys. B: At. Mol. Phys* **18**, 3811 (1985).
 - [6] R. G. DeVoe and R. G. Brewer, Observation of superradiant and subradiant spontaneous emission of two trapped ions, *Physical Review Letters* **76**, 2049 (1996).
 - [7] M. D. Barnes, P. S. Krstic, P. Kumar, A. Mehta, and J. C. Wells, Far-field modulation of fluorescence decay rates in pairs of oriented semiconducting polymer nanostructures, *Physical Review B* **71**, 241303 (2005).
 - [8] S. Filipp, A. F. van Loo, M. Baur, L. Steffen, and A. Wallraff, Preparation of subradiant states using local qubit control in circuit qed, *Physical Review A* **84**, 061805 (2011).
 - [9] B. H. McGuyer, M. McDonald, G. Z. Iwata, M. G. Tarallo, W. Skomorowski, R. Moszynski, and T. Zelevinsky, Precise study of asymptotic physics with subradiant ultracold molecules, *Nature Physics* **11**, 32 (2015).
 - [10] R. Reimann, W. Alt, T. Kampschulte, T. Macha, L. Ratschbacher, N. Thau, S. Yoon, and D. Meschede, Cavity-Modified Collective Rayleigh Scattering of Two Atoms, *Physical Review Letters* **114**, 023601 (2015), arXiv:1408.5874.
 - [11] M. Verde, A. Schaefer, B. Zenz, Z. Shehata, S. Richter, C. T. Schmiegelow, J. von Zanthier, and F. Schmidt-Kaler, Spin-selective coherent light scattering from ion crystals (2024), arXiv:2404.12513 [physics.atom-ph].
 - [12] Y. Sonnefraud, N. Verellen, H. Sobhani, G. A. Vandenbosch, V. V. Moshchalkov, P. Van Dorpe, P. Nordlander, and S. A. Maier, Experimental realization of subradiant, superradiant, and fano resonances in ring/disk plasmonic nanocavities, *ACS Nano* **4**, 1664 (2010), pMID: 20155967, <https://doi.org/10.1021/nn901580r>.
 - [13] G. Ferioli, A. Glicenstein, I. Ferrier-Barbut, and A. Browaeys, A non-equilibrium superradiant phase transition in free space, *Nature Physics* **19**, 1345 (2023).
 - [14] M. Gegg, A. Carmele, A. Knorr, and M. Richter, Superradiant to subradiant phase transition in the open system Dicke model: dark state cascades, *New Journal of Physics* **20**, 013006 (2018), arXiv:1705.02889.
 - [15] A. Shankar, J. T. Reilly, S. B. Jäger, and M. J. Holland, Subradiant-to-Subradiant Phase Transition in the Bad Cavity Laser, *Physical Review Letters* **127**, 073603 (2021), arXiv:2103.07402.
 - [16] C. Hotter, L. Ostermann, and H. Ritsch, Cavity sub- and superradiance for transversely driven atomic ensembles, *Phys. Rev. Res.* **5**, 013056 (2023).

- [17] W. Guerin, M. O. Araújo, and R. Kaiser, Subradiance in a Large Cloud of Cold Atoms, *Physical Review Letters* **116**, 083601 (2016), arXiv:1509.00227.
- [18] J. Rui, D. Wei, A. Rubio-Abadal, S. Hollerith, J. Zeiher, D. M. Stamper-Kurn, C. Gross, and I. Bloch, A subradiant optical mirror formed by a single structured atomic layer, *Nature* **583**, 369 (2020).
- [19] Z. Yan, J. Ho, Y.-H. Lu, S. J. Masson, A. Asenjo-Garcia, and D. M. Stamper-Kurn, Superradiant and subradiant cavity scattering by atom arrays, *Phys. Rev. Lett.* **131**, 253603 (2023).
- [20] A. Karnieli, N. Rivera, A. Arie, and I. Kaminer, Superradiance and subradiance due to quantum interference of entangled free electrons, *Phys. Rev. Lett.* **127**, 060403 (2021).
- [21] S. Inouye, A. P. Chikkatur, D. M. Stamper-Kurn, J. Stenger, D. E. Pritchard, and W. Ketterle, Superradiant rayleigh scattering from a bose-einstein condensate, *Science* **285**, 571 (1999).
- [22] M. M. Cola, D. Bigerni, and N. Piovella, Recoil-induced subradiance in an ultracold atomic gas, *Physical Review A* **79**, 053622 (2009).
- [23] P. Wolf, S. C. Schuster, D. Schmidt, S. Slama, and C. Zimmermann, Observation of Subradiant Atomic Momentum States with Bose-Einstein Condensates in a Recoil Resolving Optical Ring Resonator, *Physical Review Letters* **121**, 173602 (2018), arXiv:1811.02511.
- [24] K. Hepp and E. Lieb, On the superradiant phase transition for molecules in a quantized radiation field: The dicke maser model, *Annals of Physics* **76**, 360 (1973).
- [25] Y. K. Wang and F. T. Hioe, Phase transition in the dicke model of superradiance, *Physical Review A* **7**, 831 (1973).
- [26] B. M. Garraway, The dicke model in quantum optics: Dicke model revisited, *Philosophical Transactions of the Royal Society A: Mathematical, Physical and Engineering Sciences* **369**, 1137 (2011).
- [27] P. Nataf and C. Ciuti, No-go theorem for superradiant quantum phase transitions in cavity qed and counter-example in circuit qed, *Nature Communications* **1**, 72 (2010).
- [28] K. Baumann, C. Guerlin, F. Brennecke, and T. Esslinger, Dicke quantum phase transition with a superfluid gas in an optical cavity, *Nature* **464**, 1301 (2010).
- [29] H. Ritsch, P. Domokos, F. Brennecke, and T. Esslinger, Cold atoms in cavity-generated dynamical optical potentials, *Rev. Mod. Phys.* **85**, 553 (2013).
- [30] S. Schütz and G. Morigi, Prethermalization of atoms due to photon-mediated long-range interactions, *Phys. Rev. Lett.* **113**, 203002 (2014).
- [31] F. Mivehvar, F. Piazza, T. Donner, and H. Ritsch, Cavity qed with quantum gases: new paradigms in many-body physics, *Advances in Physics* **70**, 1 (2021).
- [32] N. Defenu, T. Donner, T. Macrì, G. Pagano, S. Ruffo, and A. Trombettoni, Long-range interacting quantum systems, *Rev. Mod. Phys.* **95**, 035002 (2023).
- [33] S. Fernández-Vidal, S. Zippilli, and G. Morigi, Nonlinear optics with two trapped atoms, *Phys. Rev. A* **76**, 053829 (2007).
- [34] A. Neuzner, M. Körber, O. Morin, S. Ritter, and G. Rempe, Interference and dynamics of light from a distance-controlled atom pair in an optical cavity, *Nature Photonics* **10**, 303 (2016).
- [35] I. H. Deutsch, R. J. C. Spreeuw, S. L. Rolston, and W. D. Phillips, Photonic band gaps in optical lattices, *Phys. Rev. A* **52**, 1394 (1995).
- [36] J. Barré, T. Dauxois, G. De Ninno, D. Fanelli, and S. Ruffo, Statistical theory of high-gain free-electron laser saturation, *Phys. Rev. E* **69**, 045501 (2004).
- [37] A. Campa, T. Dauxois, and S. Ruffo, Statistical mechanics and dynamics of solvable models with long-range interactions, *Physics Reports* **480**, 57 (2009).
- [38] D. Lynden-Bell, R. Wood, and A. Royal, The Gravo-Thermal Catastrophe in Isothermal Spheres and the Onset of Red-Giant Structure for Stellar Systems, *Monthly Notices of the Royal Astronomical Society* **138**, 495 (1968), <https://academic.oup.com/mnras/article-pdf/138/4/495/8078821/mnras138-0495.pdf>.
- [39] A. Morales, P. Zupancic, J. Léonard, T. Esslinger, and T. Donner, Coupling two order parameters in a quantum gas, *Nature Materials* **17**, 686 (2018), arXiv:1711.07988.
- [40] P. Zupancic, D. Dreon, X. Li, A. Baumgärtner, A. Morales, W. Zheng, N. R. Cooper, T. Esslinger, and T. Donner, P-Band Induced Self-Organization and Dynamics with Repulsively Driven Ultracold Atoms in an Optical Cavity, *Physical Review Letters* **123**, 233601 (2019), arXiv:1905.10377.
- [41] S. Zippilli, G. Morigi, and H. Ritsch, Suppression of bragg scattering by collective interference of spatially ordered atoms with a high- q cavity mode, *Phys. Rev. Lett.* **93**, 123002 (2004).
- [42] See Supplemental Material at URL-will-be-inserted-by-publisher for the data of the experiments.
- [43] R. Plestid and D. H. J. O'Dell, Balancing long-range interactions and quantum pressure: Solitons in the hamiltonian mean-field model, *Phys. Rev. E* **100**, 022216 (2019).
- [44] R. Balescu, Irreversible processes in ionized gases, *Physics of Fluids (New York)* **3**, 10.1063/1.1706002 (1960).
- [45] M. Henon, Vlasov equation, *Astron. Astrophys.* **114**, 211 (1982).
- [46] P. Bertrand, D. Sarto, and A. Ghizzo, *The Vlasov Equation 1: History and General Properties* (Wiley, 2019).
- [47] Y. Elskens and M. K. H. Kiessling, Microscopic foundations of kinetic plasma theory: The relativistic vlasov-maxwell equations and their radiation-reaction-corrected generalization, *Journal of Statistical Physics* **180**, 749 (2020).
- [48] S. Schütz, S. B. Jäger, and G. Morigi, Dissipation-assisted prethermalization in long-range interacting atomic ensembles, *Phys. Rev. Lett.* **117**, 083001 (2016).
- [49] D. Lynden-Bell, Statistical Mechanics of Violent Relaxation in Stellar Systems, *Monthly Notices of the Royal Astronomical Society* **136**, 101 (1967), <https://academic.oup.com/mnras/article-pdf/136/1/101/8075239/mnras136-0101.pdf>.

- [50] K. Jain, F. Bouchet, and D. Mukamel, Relaxation times of unstable states in systems with long range interactions, *Journal of Statistical Mechanics: Theory and Experiment* **2007**, P11008 (2007).
- [51] F. Bouchet and J. Barré, Statistical mechanics of systems with long range interactions, *Journal of Physics: Conference Series* **31**, 18 (2006).
- [52] M. Antoni and S. Ruffo, Clustering and relaxation in hamiltonian long-range dynamics, *Phys. Rev. E* **52**, 2361 (1995).
- [53] N. Defenu, Metastability and discrete spectrum of long-range systems, *Proceedings of the National Academy of Sciences* **118**, 1 (2021), arXiv:2012.15808.
- [54] S. Gupta and D. Mukamel, Slow relaxation in long-range interacting systems with stochastic dynamics, *Phys. Rev. Lett.* **105**, 040602 (2010).
- [55] M. C. Braidotti, M. Lovisetto, R. Prizia, C. Michel, C. Didier, M. Bellec, E. M. Wright, B. Marcos, and D. Faccio, Experimental observation of violent relaxation, *Communications Physics* **7**, 206 (2024).
- [56] Z. Wu, J. Fan, X. Zhang, J. Qi, and H. Wu, Signatures of prethermalization in a quenched cavity-mediated long-range interacting fermi gas, *Phys. Rev. Lett.* **131**, 243401 (2023).
- [57] T. Zwettler, G. del Pace, F. Marijanovic, S. Chattopadhyay, T. Bühler, C.-M. Halati, L. Skolc, L. Tolle, V. Helson, G. Bolognini, A. Fabre, S. Uchino, T. Giamarchi, E. Demler, and J.-P. Brantut, Non-equilibrium dynamics of long-range interacting fermions (2024), arXiv:2405.18204 [cond-mat.quant-gas].
- [58] F. Marijanović, S. Chattopadhyay, L. Skolc, T. Zwettler, C.-M. Halati, S. B. Jäger, T. Giamarchi, J.-P. Brantut, and E. Demler, Dynamical instabilities of strongly interacting ultracold fermions in an optical cavity (2024), arXiv:2406.13548 [cond-mat.quant-gas].
- [59] D. A. Steck, Rubidium 87 d line data, <https://steck.us/alkalidata/rubidium87numbers.pdf> (2001), accessed: 8th July, 2024.
- [60] S. B. Jäger, T. Schmit, G. Morigi, M. J. Holland, and R. Betzholtz, Lindblad master equations for quantum systems coupled to dissipative bosonic modes, *Phys. Rev. Lett.* **129**, 063601 (2022).
- [61] T. Schmit and et al, preprint (2024).
- [62] J. Larson, S. Fernández-Vidal, G. Morigi, and M. Lewenstein, Quantum stability of mott-insulator states of ultracold atoms in optical resonators, *New Journal of Physics* **10**, 045002 (2008).
- [63] S. Schütz, H. Habibian, and G. Morigi, Cooling of atomic ensembles in optical cavities: Semiclassical limit, *Phys. Rev. A* **88**, 033427 (2013).
- [64] S. Krämer, D. Plankensteiner, L. Ostermann, and H. Ritsch, Quantumoptics.jl: A julia framework for simulating open quantum systems, *Computer Physics Communications* **227**, 109 (2018).
- [65] S. B. Jäger, J. Cooper, M. J. Holland, and G. Morigi, Dynamical phase transitions to optomechanical superradiance, *Phys. Rev. Lett.* **123**, 053601 (2019).
- [66] A. Morales, D. Dreon, X. Li, A. Baumgärtner, P. Zupancic, T. Donner, and T. Esslinger, Two-mode dicke model from nondegenerate polarization modes, *Physical Review A* **100**, 013816 (2019).
- [67] X. Li, D. Dreon, P. Zupancic, A. Baumgärtner, A. Morales, W. Zheng, N. R. Cooper, T. Donner, and T. Esslinger, First order phase transition between two centro-symmetric superradiant crystals, *Physical Review Research* **3**, L012024 (2021).